

Supplementary Materials for  
**Room-temperature quantum coherence of entangled multiexcitons in a  
metal-organic framework**

Akio Yamauchi *et al.*

Corresponding author: Yasuhiro Kobori, [ykobori@kitty.kobe-u.ac.jp](mailto:ykobori@kitty.kobe-u.ac.jp); Kiyoshi Miyata,  
[kmiyata@chem.kyushu-univ.jp](mailto:kmiyata@chem.kyushu-univ.jp); Nobuhiro Yanai, [yanai@mail.cstm.kyushu-u.ac.jp](mailto:yanai@mail.cstm.kyushu-u.ac.jp)

*Sci. Adv.* **10**, eadi3147 (2024)  
DOI: 10.1126/sciadv.adi3147

**The PDF file includes:**

Supplementary Text  
Figs. S1 to S19  
Tables S1 to S5  
References

## Electron spin polarization model considering the molecular motions and exciton migrations in the TT and T+T states in the multiexciton.

From the spin-correlated triplet pair model, coupled stochastic-Liouville equation can be described in  ${}^5(\text{TT})_{mS} - {}^3(\text{TT})_m - {}^1(\text{TT})$  three-level systems where  $m_S = +2, +1, 0, -1, -2$ , and  $m = +1, 0, -1$ , assuming that the quintet-triplet and the singlet-triplet interconversions are ignored in the strongly coupled TT states. The quintet-triplet-singlet (Q-T-S) mixings are considered in the T+T states. In the strongly coupled TT,  ${}^5(\text{TT})_{mS} - {}^1(\text{TT})$  two level system is considered for the quintet generation. For  $m_S = \pm 1$ ,  ${}^3(\text{TT})_m$  with  $m = \pm 1$  participate in the Q-T-S mixings, respectively, as the three-level systems in the T+T. For  $m_S = 0$ ,  ${}^5(\text{TT})_0 - {}^3(\text{TT})_0 - {}^1(\text{TT})$  mixing may occur in the T+T. This is because  ${}^5(\text{TT})_0$ ,  ${}^3(\text{TT})_0$  and  ${}^1(\text{TT})$  diabatic levels are very close each other for the small exchange coupling in the presence of the strong external magnetic field. The following relations are thus obtained, based upon a previous report: (51)

$$\begin{aligned} \dot{\rho}_{\text{TT1}} = & -i \left[ \begin{pmatrix} E_{Q_{ms}}^{\text{TT1}} & 0 \\ 0 & E_S^{\text{TT1}} \end{pmatrix}, \rho_{\text{TT1}} \right] - k_{12} \rho_{\text{TT1}} + k_{21} \rho_{\text{TT2}} - k_{\text{DISS}} \rho_{\text{TT1}} \\ & - \begin{pmatrix} 0 & \frac{k_{\text{REC}} \rho_{Q_{ms}S}^{\text{TT1}}}{2} \\ \frac{k_{\text{REC}} \rho_{SQ_{ms}}^{\text{TT1}}}{2} & k_{\text{REC}} \rho_{SS}^{\text{TT1}} \end{pmatrix} + k_{\text{Back}} \rho_{\text{T+T}} \end{aligned} \quad (\text{S1})$$

$$\dot{\rho}_{\text{TT2}} = -i \left[ \begin{pmatrix} H_{Q_{ms}Q_{ms}}^{\text{TT2}} & H_{Q_{ms}S}^{\text{TT2}} \\ H_{SQ_{ms}}^{\text{TT2}} & H_{SS}^{\text{TT2}} \end{pmatrix}, \rho_{\text{TT2}} \right] + k_{12} \rho_{\text{TT1}} - k_{21} \rho_{\text{TT2}} \quad (\text{S2})$$

$$\begin{aligned} \dot{\rho}_{\text{T+T}} = & -i \left[ \begin{pmatrix} H_{Q_{ms}Q_{ms}}^{\text{T+T}} & H_{Q_{ms}T_m}^{\text{T+T}} & H_{Q_{ms}S}^{\text{T+T}} \\ H_{T_mQ_{ms}}^{\text{T+T}} & H_{T_mT_m}^{\text{T+T}} & H_{T_mQ_{ms}}^{\text{T+T}} \\ H_{SQ_{ms}}^{\text{T+T}} & H_{Q_{ms}T_m}^{\text{T+T}} & H_{SS}^{\text{T+T}} \end{pmatrix}, \rho_{\text{T+T}} \right] + k_{\text{DISS}} \rho_{\text{TT1}} - k_{\text{Back}} \rho_{\text{T+T}} \\ & - \begin{pmatrix} 0 & k_T \rho_{Q_{ms}T_m}^{\text{T+T}}/2 & k_S \rho_{Q_{ms}S}^{\text{T+T}}/2 \\ k_T \rho_{T_mQ_{ms}}^{\text{T+T}}/2 & k_T \rho_{T_mT_m}^{\text{T+T}} & (k_S + k_T) \rho_{T_mS}^{\text{T+T}}/2 \\ k_S \rho_{SQ_{ms}}^{\text{T+T}}/2 & (k_S + k_T) \rho_{ST_m}^{\text{T+T}}/2 & k_S \rho_{SS}^{\text{T+T}} \end{pmatrix} \end{aligned} \quad (\text{S3})$$

where superscripts in the density matrices represent the strongly-coupled TT<sub>1</sub> with large  $J_1$ , the thermally activated TT<sub>2</sub> with the intermediate coupling of  $J_2 \approx -10$  GHz, and the decoupled T+T site, respectively.  $E_{Q_{ms}}$  and  $E_S$  are the eigenenergies in TT<sub>1</sub>. In the subscripts,  ${}^5(\text{TT})_{mS} = Q_{mS}$ , and  ${}^1(\text{TT}) = S$  are attributable.  $H_{Q_{ms}Q_{ms}}$ ,  $H_{Q_{ms}S}$ ,  $H_{SQ_{ms}}$  and  $H_{SS}$  are respective diagonal and off-diagonal terms of the spin Hamiltonians ( $\mathbf{H}_{\text{TT2}}$ , and  $\mathbf{H}_{\text{T+T}}$ ) on the basis spin system of  ${}^5(\text{TT})_{mS}$  and  ${}^1(\text{TT})$  in the TT<sub>1</sub> state.  $k_{12}$  and  $k_{21}$  are site exchange rate constants determined by the vibration frequency ( $\bar{\nu}_{\text{vib}}$ ) between TT<sub>1</sub> and TT<sub>2</sub> sites with  $k_{12} =$

$k_{21}\exp(-\Delta E_{12}/k_B T)$ .  $k_{\text{DISS}}$  and  $k_{\text{Back}}$  represent the T+T dissociation rate, and the back-reaction rate from the T+T state to the TT<sub>1</sub> state, respectively.  $k_T$  and  $k_S$  represent recombination rates from the T+T states via the singlet and triplet characters, respectively.  $k_T = k_S = 10^5 \text{ s}^{-1}$  was assumed in the present calculations. The density matrices are thus represented, as follows.

$$\rho_{\text{TT1}} = \begin{pmatrix} \rho_{Q_{m_S}Q_{m_S}}^{\text{TT1}} & \rho_{Q_{m_S}S}^{\text{TT1}} \\ \rho_{SQ_{m_S}}^{\text{TT1}} & \rho_{SS}^{\text{TT1}} \end{pmatrix} \quad (\text{S4})$$

$$\rho_{\text{TT2}} = \begin{pmatrix} \rho_{Q_{m_S}Q_{m_S}}^{\text{TT2}} & \rho_{Q_{m_S}S}^{\text{TT2}} \\ \rho_{SQ_{m_S}}^{\text{TT2}} & \rho_{SS}^{\text{TT2}} \end{pmatrix} \quad (\text{S5})$$

$$\rho_{\text{T+T}} = \begin{pmatrix} \rho_{Q_{m_S}Q_{m_S}}^{\text{T+T}} & \rho_{Q_{m_S}T_m}^{\text{T+T}} & \rho_{Q_{m_S}S}^{\text{T+T}} \\ \rho_{T_mQ_{m_S}}^{\text{T+T}} & \rho_{T_mT_m}^{\text{T+T}} & \rho_{T_mS}^{\text{T+T}} \\ \rho_{SQ_{m_S}}^{\text{T+T}} & \rho_{ST_m}^{\text{T+T}} & \rho_{SS}^{\text{T+T}} \end{pmatrix} \quad (\text{S6})$$

Coupled time-differential equations in the 12 (for  $m_S = \pm 2$  with S) or 17 (for  $m_S = \pm 1$  or 0 with  $m = \pm 1$  or with  $m = 0$ ) elements in eqs. (S15)-(S17) are described by regenerating a  $\vec{\rho}$  vector composed of these elements. Then, the following master equation is obtained:

$$\frac{\partial \vec{\rho}}{\partial t} = \mathbf{L} \vec{\rho} \quad (\text{S7})$$

where  $\mathbf{L}$  is summarized in Tables S1, S2. In these tables,  $\rho_{QQ1} = \rho_{Q_{m_S}Q_{m_S}}^{\text{TT1}}$ ,  $\rho_{QS1} = \rho_{Q_{m_S}S}^{\text{TT1}}$ ,  $\rho_{SQ1} = \rho_{SQ_{m_S}}^{\text{TT1}}$ ,  $\rho_{SS1} = \rho_{SS}^{\text{TT1}}$ ,  $\rho_{QQ2} = \rho_{Q_{m_S}Q_{m_S}}^{\text{TT2}}$ ,  $\rho_{QS2} = \rho_{Q_{m_S}S}^{\text{TT2}}$ ,  $\rho_{SQ2} = \rho_{SQ_{m_S}}^{\text{TT2}}$ ,  $\rho_{SS2} = \rho_{SS}^{\text{TT2}}$ ,  $\rho_{QQ(\text{T+T})} = \rho_{Q_{m_S}Q_{m_S}}^{\text{T+T}}$ ,  $\rho_{QT(\text{T+T})} = \rho_{Q_{m_S}T_m}^{\text{T+T}}$ ,  $\rho_{QS(\text{T+T})} = \rho_{Q_{m_S}S}^{\text{T+T}}$ ,  $\rho_{TQ(\text{T+T})} = \rho_{T_mQ_{m_S}}^{\text{T+T}}$ ,  $\rho_{TT(\text{T+T})} = \rho_{T_mT_m}^{\text{T+T}}$ ,  $\rho_{TS(\text{T+T})} = \rho_{T_mS}^{\text{T+T}}$ ,  $\rho_{SQ(\text{T+T})} = \rho_{SQ_{m_S}}^{\text{T+T}}$ ,  $\rho_{ST(\text{T+T})} = \rho_{ST_m}^{\text{T+T}}$ ,  $\rho_{SS(\text{T+T})} = \rho_{SS}^{\text{T+T}}$  are attributable in eqs.(S4)-(S6).

From eq.(S6), the nine adiabatic-state populations ( $\rho^{\text{T+T}}_{ii}$ ) where  $i = 1, 2, \dots, 9$  in the dissociated multiexciton is obtained from the diagonal terms of  $\rho_{1-9}^{\text{T+T}} = \mathbf{U}_{\text{T+T}}^t \rho^{\text{T+T}} \mathbf{U}_{\text{T+T}}$  in the SCTP eigenstates calculated by the eigenvectors  $\mathbf{U}_{\text{T+T}}$  obtained by diagonalizing the spin Hamiltonian of  $\mathbf{H}_{\text{T+T}}$ , where,



In eq.(S11),  $\langle i|\hat{S}_y|k\rangle^2$ ,  $\varepsilon_i$  and  $\varepsilon_k$  are obtained from the eigenvectors  $\mathbf{U}_{T+T}$  and the eigenvalues by diagonalizing the spin Hamiltonian of  $\mathbf{H}_{T+T}$  to determine the eigenstates of  $|i\rangle = \sum_j^9 c_{ij} |TT\rangle_j$ .

In the zero-field splitting interaction of  $\mathbf{H}_{TTzfs}$  ( $= \mathbf{S}_1\mathbf{D}_1\mathbf{S}_1 + \mathbf{S}_2\mathbf{D}_2\mathbf{S}_2$ ),  $\mathbf{S}_i$  is the  $i$ -th triplet spin operator ( $i = 1$  and  $2$  for A and B moieties, respectively in the  $T_A T_B$  multiexciton), and  $\mathbf{D}_i$  represents the ZFS tensor of the individual triplet. The matrix of the  $\mathbf{H}_{TTzfs}$  tensor is dependent on the orientation of the principal axes in the  $\mathbf{D}_2$  tensor ( $X_2, Y_2, Z_2$ ) with respect to the principal axes in  $\mathbf{D}_1$  tensor ( $X_1, Y_1, Z_1$ ), the geometries of the second pentacene groups were generated by using Euler rotation angles ( $\alpha, \beta, \gamma$ ) with respect to the principal axes in  $\mathbf{D}_i$  as follows.

$$\mathbf{D}_1 = \begin{pmatrix} -\frac{D}{3} + E & & \\ & -\frac{D}{3} - E & \\ & & 2D/3 \end{pmatrix}, \text{ and } \mathbf{D}_2 = \mathbf{R}\mathbf{D}_1\mathbf{R} \quad (\text{S13})$$

$$\text{with } \mathbf{R} = \begin{pmatrix} \cos\gamma & \sin\gamma & \\ -\sin\gamma & \cos\gamma & \\ & & 1 \end{pmatrix} \begin{pmatrix} 1 & & \\ & \cos\beta & \sin\beta \\ & -\sin\beta & \cos\beta \end{pmatrix} \begin{pmatrix} \cos\alpha & \sin\alpha & \\ -\sin\alpha & \cos\alpha & \\ & & 1 \end{pmatrix} \quad (\text{S14})$$

Direction for the second triplet-state position in TT was set by the polar angles ( $\theta_2$  and  $\phi_2$ ) with respect the ( $X_1, Y_1, Z_1$ ) principal axes. The direction of the external magnetic field ( $\mathbf{B}_0$ ) was set by the polar angles ( $\theta, \phi$ ). Thus,  $\cos^2\theta_D$  where  $\theta_D$  is the angle between  $\mathbf{B}_0$  and the inter-spin vector as the principal axis in  $\mathbf{H}_{TTss} = D_{SS}(\cos^2\theta_D - 1/3)(3\mathbf{S}_{1Z}\mathbf{S}_{2Z} - \mathbf{S}_1\mathbf{S}_2)$  is defined for each  $\mathbf{B}_0$  direction, as reported previously.

### Computation method of the transverse magnetization in the pulsed EPR measurements:

The nutation profiles and the echo-detected field swept spectrum of the triplet pair are computed from the expectation values of the transverse magnetization of  $\langle S_y \rangle$  in the quintet wavefunctions based upon the report by Gierer et al. (52) on the radical pairs. After the pulse durations of  $x$  (s) and  $t_2$  (s) in the first and second pulses, respectively in Fig. 6A,  $\langle S_y(\tau_{delay}, x) \rangle$  is represented for a specific field direction, as follows:

$$\begin{aligned} \langle S_y(\tau_{delay}, x) \rangle = & \sum_{m_S=-2,-1,0,+1} I_{m_S, m_S+1}(\tau_{delay}) \left( \frac{\omega_{m_S}}{\omega'_{m_S}} \right)^2 \sin\{\omega'_{m_S} x\} \cos\{\omega'_{m_S} t_2\} \\ & \times \exp \left[ -\frac{x}{T_{2D}} \left\{ 1 - \frac{1}{2} \left( \frac{\omega_{m_S}}{\omega'_{m_S}} \right)^2 \right\} \right] \end{aligned} \quad (S15)$$

with

$$I_{m_S, m_S+1}(\tau_{delay}) = \rho_{m_S, m_S+1}^{TT1}(\tau_{delay}) + \rho_{m_S, m_S+1}^{TT2}(\tau_{delay}) \quad (S16)$$

where

$$\begin{aligned} & \begin{bmatrix} \rho_{m_S, m_S+1}^{TT1}(\tau_{delay}) \\ \rho_{m_S, m_S+1}^{TT2}(\tau_{delay}) \end{bmatrix} = \\ & \left( \begin{array}{cc} \left( -\omega_0 - E_{Q_{m_S}}^{TT1} + E_{Q_{m_S+1}}^{TT1} \right) - i \left( k_{12} + \frac{1}{T_{2Q}} \right) & ik_{21} \\ ik_{12} & \left( -\omega_0 - E_{Q_{m_S}}^{TT2} + E_{Q_{m_S+1}}^{TT2} \right) - i \left( k_{21} + \frac{1}{T_{2Q}} \right) \end{array} \right)^{-1} \times \\ & \begin{bmatrix} -\rho_{m_S, m_S}^{TT1}(\tau_{delay}) + \rho_{m_S+1, m_S+1}^{TT1}(\tau_{delay}) \\ -\rho_{m_S, m_S}^{TT2}(\tau_{delay}) + \rho_{m_S+1, m_S+1}^{TT2}(\tau_{delay}) \end{bmatrix} \exp \left( -\frac{\tau_{delay}}{T_1} \right) \end{aligned} \quad (S17)$$

and

$$\omega'_{m_S} = \sqrt{\omega_{m_S}^2 + \left( -\omega_0 - E_{Q_{m_S}}^{TT1,2} + E_{Q_{m_S+1}}^{TT1,2} \right)^2} \quad (S18)$$

$\omega_0$  is the angular frequency of the microwave.

Equations S15 and S16 represent y-magnetization responses by the first and second microwaves with an angular frequency of  $\omega_0$  in the quintet states those of which are in equilibrium between  $TT_1$  and  $TT_2$  states, as detailed in the previous studies in dimer systems. Method to compute the sublevel populations  $[\rho_{m_S, m_S}^{TT1}(\tau_{delay})$  and  $\rho_{m_S, m_S}^{TT2}(\tau_{delay})]$  after the SF and sublevel energies ( $E_{Q_{m_S}}^{TT1}$  and  $E_{Q_{m_S}}^{TT2}$ ) in the presence of the external magnetic field are detailed in the previous reports (20, 51).  $T_{2D} = 150$  ns and  $T_1 = 3.8$   $\mu$ s are employed as the decoherence time and the spin-lattice relaxation time in Equations S15 and S17, respectively.  $k_{12}$  and  $k_{21}$  represent rate constants of the conformational changes between  $TT_1$  and  $TT_2$ . It is

noted that such quick conformation changes themselves do not induce the decoherences in  $\rho_{m_S m_{S+1}}^{\text{TT1}}$  and  $\rho_{m_S m_{S+1}}^{\text{TT2}}$  because the nutation frequency of the quintet EPR transitions in eq. 1 is not altered by the exchange process with  $k_{12}$  and  $k_{21}$ . The echo signals are thus obtained as follows:

$$\text{Echo}(\tau_{\text{delay}}, x) = - \int_0^\pi \int_0^\pi \text{imag}\langle S_y(\tau_{\text{delay}}, x) \rangle \sin \theta \, d\theta \, d\phi \quad (\text{S19})$$

where  $\theta$  and  $\phi$  are the polar and azimuth angles of the external magnetic field applied with respect to the principal axis system in the  $T_A$  triplet in the zero-field splitting interaction (Fig. S19A). In eq. (S15), the off-resonance effect described in the parentheses is ignored because of the largely reduced y-magnetization response when  $T_{2Q} = 100$  ns is applied at the off-resonance in eq. (S3). This may correspond to the sharp angle selectivity of the quantum gate (Fig. S19A) at the specific field position of  $B_0 = 348.1$  mT for the sharp resonance polarization in Fig. 6C. However, minor off-resonance effects are included in the nutation components of 31 and 25 MHz in Fig. 6D considering that the nutation frequency of the radical is 12 MHz in Fig. S16, because 31 and 25 MHz in Fig. 6D are slightly higher than  $\sqrt{6} \times 12 (= 29)$  and  $2 \times 12 (= 24)$  MHz, respectively.

The red spectrum in Fig. 6C shows the computed echo signal of eq. (S15) at  $\tau_{\text{delay}} = 1.1 \mu\text{s}$  with substituting  $x = 5$  ns and  $t_2 = 13$  ns as a function of the external magnetic field  $B_0$ . For the nutation profiles in Figs. 6E and 6F, eq. (S15) is plotted as a function of  $x$  for  $\tau_{\text{delay}} = 1.1 \mu\text{s}$  at  $B_0 = 348.1$  mT applying  $t_2 = 16$  ns. For the delay time dependence of the echo signal (Fig. 6F), the echo signal of eq. (S15) is plotted as a function of  $\tau_{\text{delay}}$  at the field position of 352 mT.

We also mapped the initial response function of eq. (S16) to all the field directions to visualize angle selectivity of the y-magnetization for all the four quantum gates. (Fig. S19)

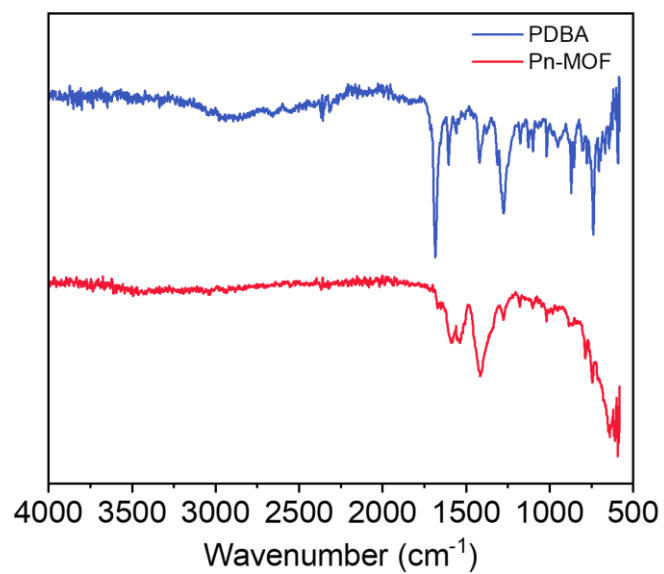


**Fig. S1. FT-IR spectra of PDBA (blue line) and Pn-MOF (red line) obtained at room temperature.**

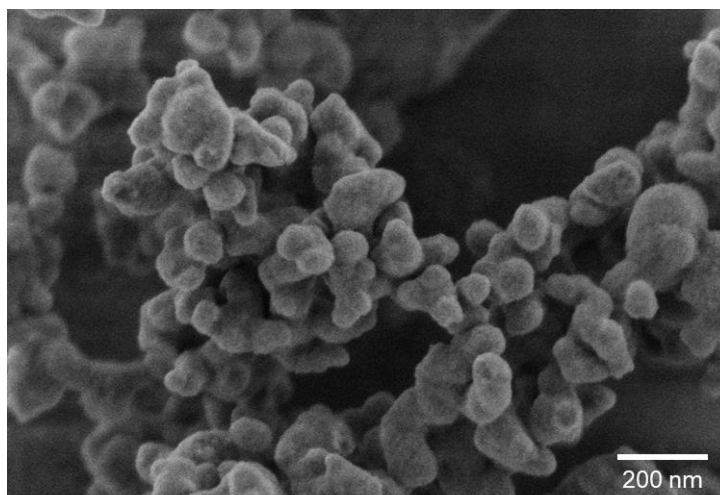


**Fig. S2. SEM image of Pn-MOF.**

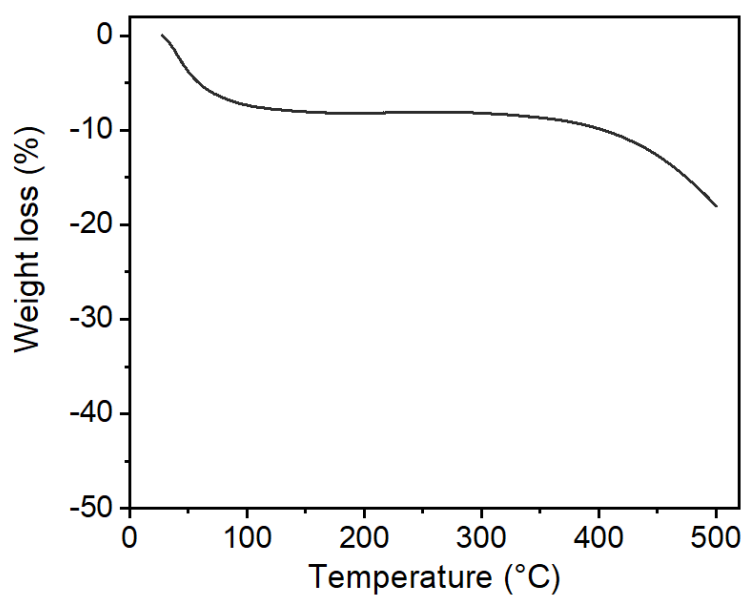


**Fig. S3. TGA curve of Pn-MOF under N<sub>2</sub> atmosphere.** The heating rate of the measurement was 5 °C/min. Weight loss below 100 °C is attributed to the uptake of water from the air into the pores of the Pn-MOF.

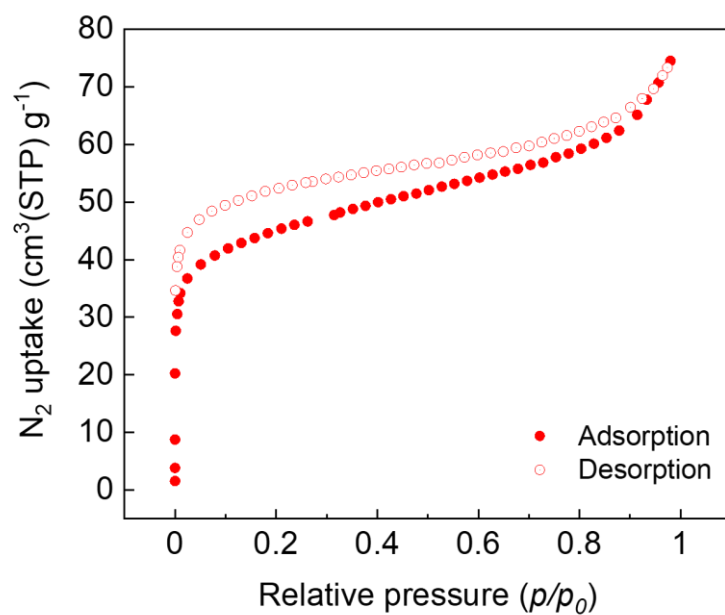


**Fig. S4. Nitrogen adsorption isotherm of Pn-MOF at 77 K.** The filled circle represents the adsorption and open circle represents desorption.

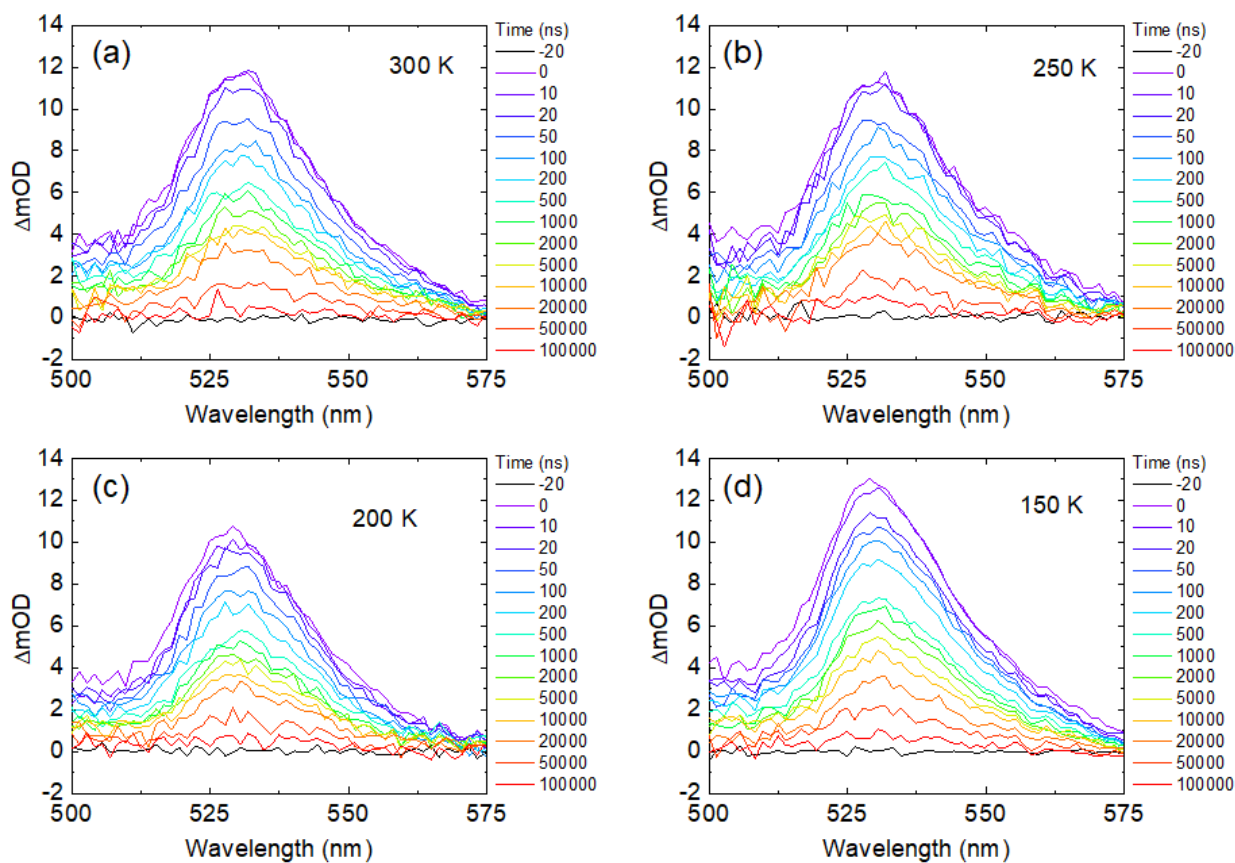


**Fig. S5. Transient absorption spectra of Pn-MOF at different temperatures.** (a) 300 K, (b) 250 K, (c) 200 K, (d) 150 K. The TAS spectra in this spectral range are insensitive to spin multiplicity, as no substantial spectral change was observed.

## Dynamic conformation model in $\beta$

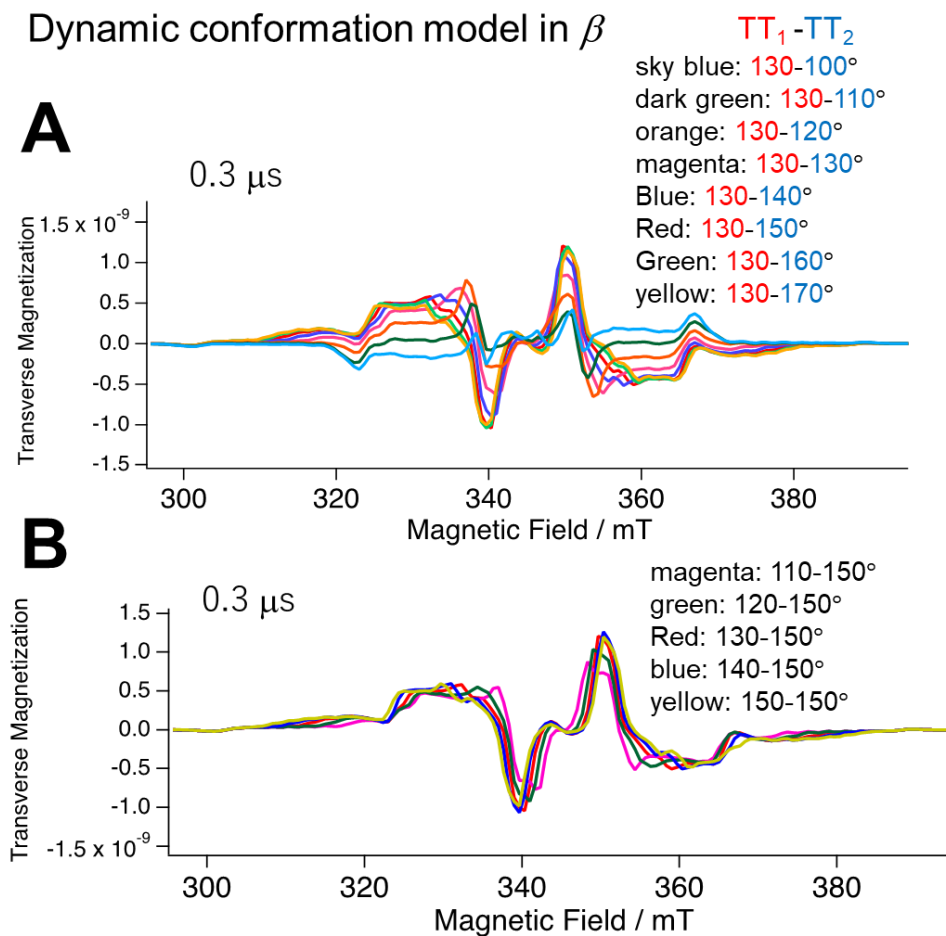


**Fig. S6. Effects of the conformation angles.** Effects of the conformation angles of  $\beta$  in the  $TT_1$  (red) and  $TT_2$  (blue) on the spin-polarized EPR spectra of the multiexcitons at the delay time of 0.3  $\mu\text{s}$ . The other parameters are fixed and are listed in Table S3.

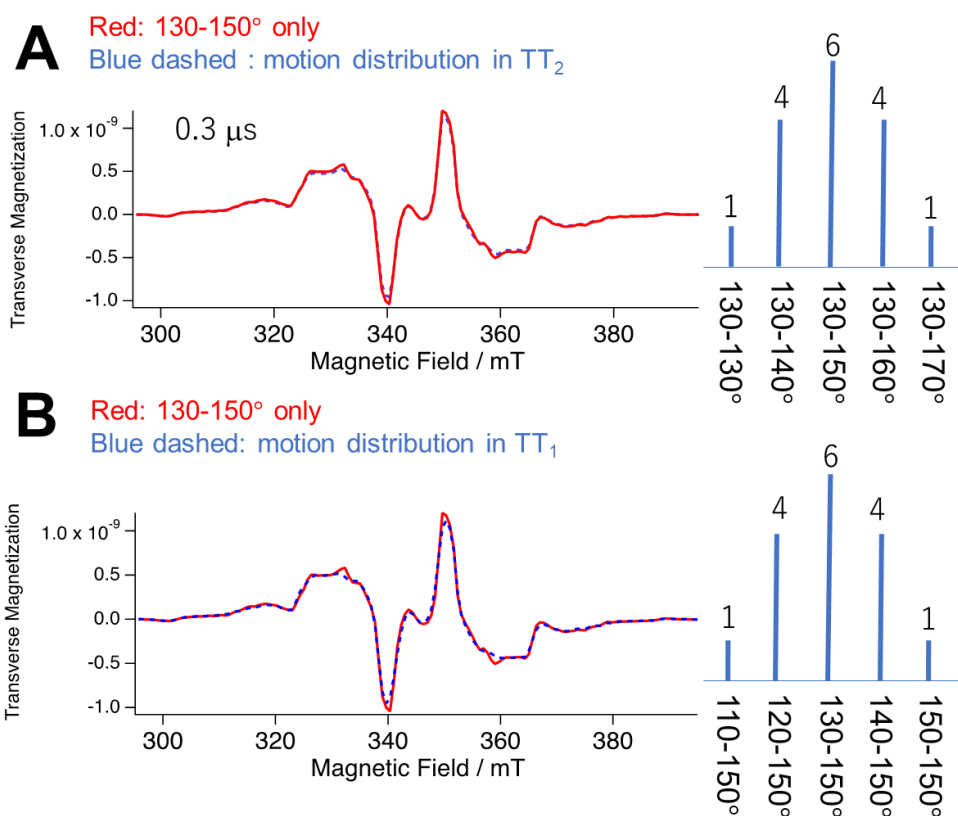


**Fig. S7. Comparisons between the computed EPR spectra.** Comparisons between the computed EPR spectra obtained by considering the conformation change between TT<sub>1</sub> ( $\beta=130$  degrees) and TT<sub>2</sub> (150 degrees) in the red solid lines and spectra (blue dashed lines) obtained by summing the data in Fig. S6 with weighting 1:4:6:4:1 amplitudes for  $\beta=130, 140, 150, 160$  and 170 degrees in the TT<sub>2</sub> in (A) and with the 1:4:6:4:1 amplitudes for  $\beta=110, 120, 130, 140$  and 150 degrees in the TT<sub>1</sub> in (B). The bars in the right represent the distributions of the molecular conformations to obtain the dashed lines.

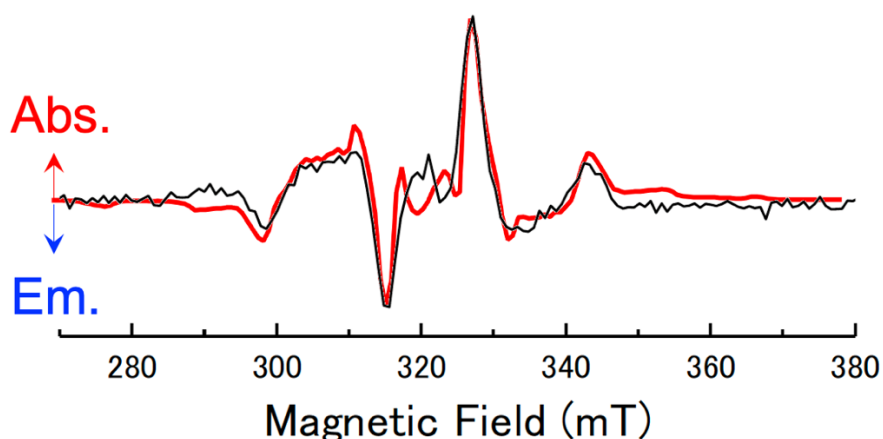


**Fig. S8. Time-resolved EPR spectra of Pn-MOF in paraffin at 150 K obtained at 1  $\mu$ s after the laser pulse.** The measurements were carried out using a home-built X-band ( $\sim$ 9 GHz) dielectric resonator with a window for laser irradiation at a magnetic field generated by an electromagnet. Samples were photoexcited by using a pulsed laser (Tolar-527, Beamtech Optronics). Wavelength, repetition rate, and pulse energy were 527 nm, 100 Hz, and 2~3 mJ/pulse, respectively. An electromagnet was purchased from Takano (MC160A-16). The gap and the pole size were 50 mm and 120 mm, respectively. A power supply PAG60-55 (Kikusui) with the stability of  $10^{-4}$  was used. A microwave was generated from SG22000Pro (DS instruments) with the power of  $\sim$ 10  $\mu$ W. The EPR signal was converted to DC using diode detector, amplified with a low noise amp (ALN0905-12-3010, Dynamic RF Inc.), and detected by an oscilloscope (DSOX3024T, Keysight). The samples were put into capillaries and measured at 150 K. The red line is obtained by the rotation model analysis in Fig. 5 using the parameters in Table S3 that explained the TAS profile in Fig. 4C.

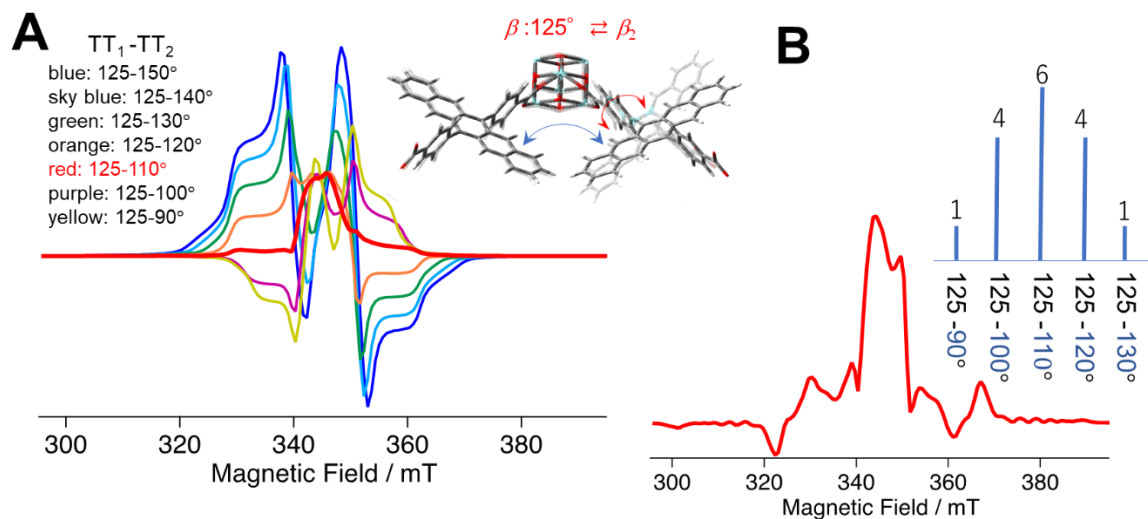


**Fig. S9. Quintet EPR spectra computed by several  $TT_2$  conformations.** (A) Spin polarized quintet EPR spectra at 0.1  $\mu$ s computed by several  $TT_2$  conformations. (B) Averaged spectrum considering the distribution in the  $TT_2$  conformations.

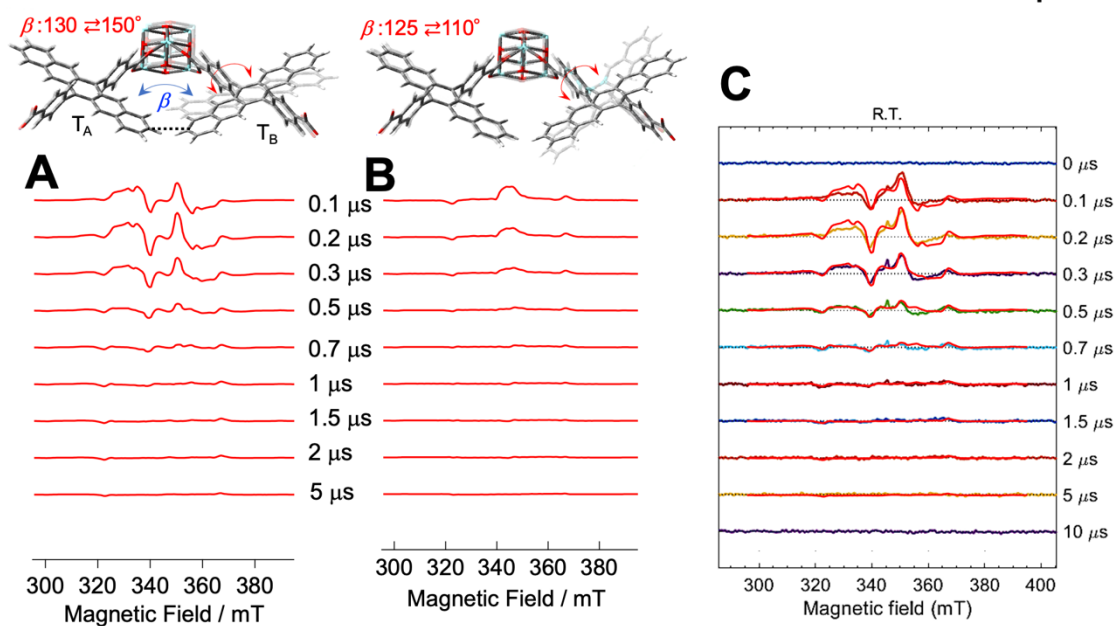


**Fig. S10. Computed time evolution of the transverse magnetization spectrum.** (A) Computed time evolution of the transverse magnetization spectrum using the conformation model between  $\beta = 130$  degrees and  $150$  degrees. (B) Computed time evolution of the transverse magnetization spectrum with using the motion between  $\beta = 125$  degrees and  $110$  degrees. (C) Red computed spectra are obtained by adding the data (B) to (A). Note that the time dependence of the transient EPR spectrum in Figure S10B is obtained using the same kinetic parameters of  $k_{\text{Diss}} = 3.0 \times 10^6 \text{ (s}^{-1}\text{)}$ ,  $k_{\text{Back}} = 1.1 \times 10^6 \text{ (s}^{-1}\text{)}$  and  $k_{\text{Rec}} = 5.6 \times 10^7 \text{ (s}^{-1}\text{)}$  as used for Figure S10A (Table S3, 300 K), denoting that the ns-TA decay in Fig. 4C is unaffected by incorporating the different conformation dynamics.

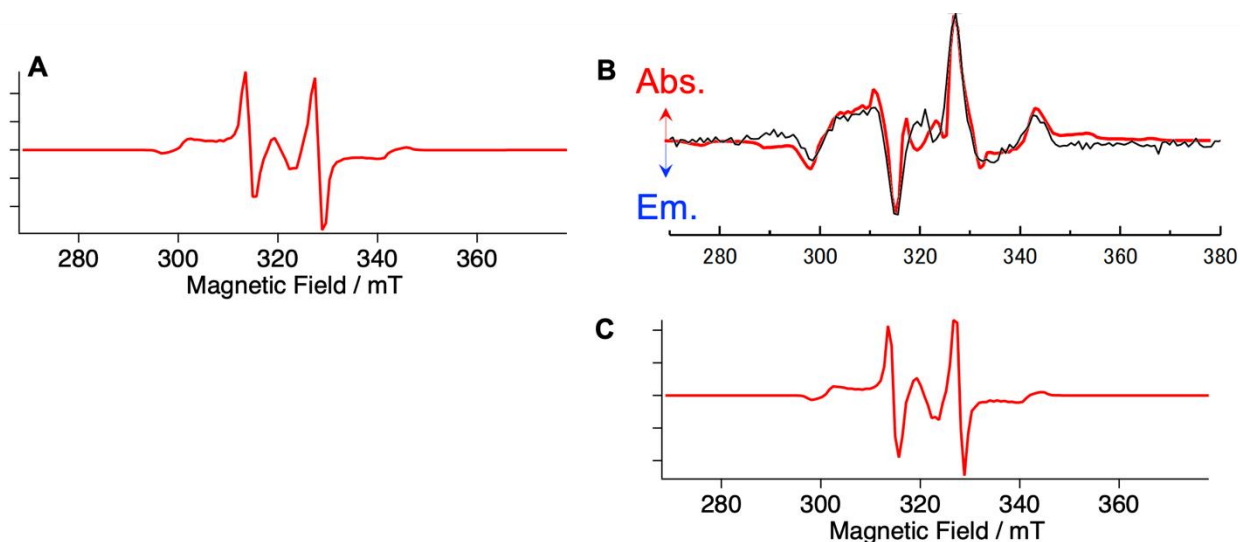


**Fig. S11. Reproduction of previously reported spectra and comparison with the present spectra.** (A) Computed spin polarized EPR spectrum of the quintet TT state of the tetracene dimer (TIPS-BP1') conformationally defined by the rigid linkage in doi.org/10.1038/s41467-023-36529-6 (14). The calculation is performed using the sublevel populations obtained at 0.2  $\mu$ s in the TT<sub>1</sub> state considering the J-modulation between  $J_1 = 1.4 \times 10^6$  MHz and  $J_2 = -5.6 \times 10^4$  MHz with a common T<sub>A</sub>T<sub>B</sub> conformation defined by  $(\alpha, \beta, \gamma) = (0^\circ, 111^\circ, 0^\circ)$  and  $(\theta_2, \phi_2) = (70^\circ, -90^\circ)$  in the TT<sub>1</sub> and TT<sub>2</sub> states with  $D = 1322$  MHz and  $D_{SS} = -55$  MHz. These angle parameters are characterized as the T<sub>B</sub> conformations with respect to the principal axis system of the T<sub>A</sub> in the T<sub>A</sub>T<sub>B</sub> multiexciton and are consistent with the reported dimer geometry. This spin-polarized EPR spectrum demonstrates validity and compatibility of the present numerical model with the reported theory in doi.org/10.1038/s41467-023-36529-6 (14). (B) Same as Fig. S8 observed at 150 K in the present MOF sample. (C) Computed spin polarized EPR spectrum of the quintet TT state for the pentacene dimer obtained with  $D = 1265$  MHz and  $D_{SS} = -55$  MHz. The other parameters are identical with those for (A). The better fit is obtained based upon the structure in Fig. 4B as an average dihedral angle ( $140^\circ$ ) between  $\beta = 164^\circ$  and  $113^\circ$  in Table S3.

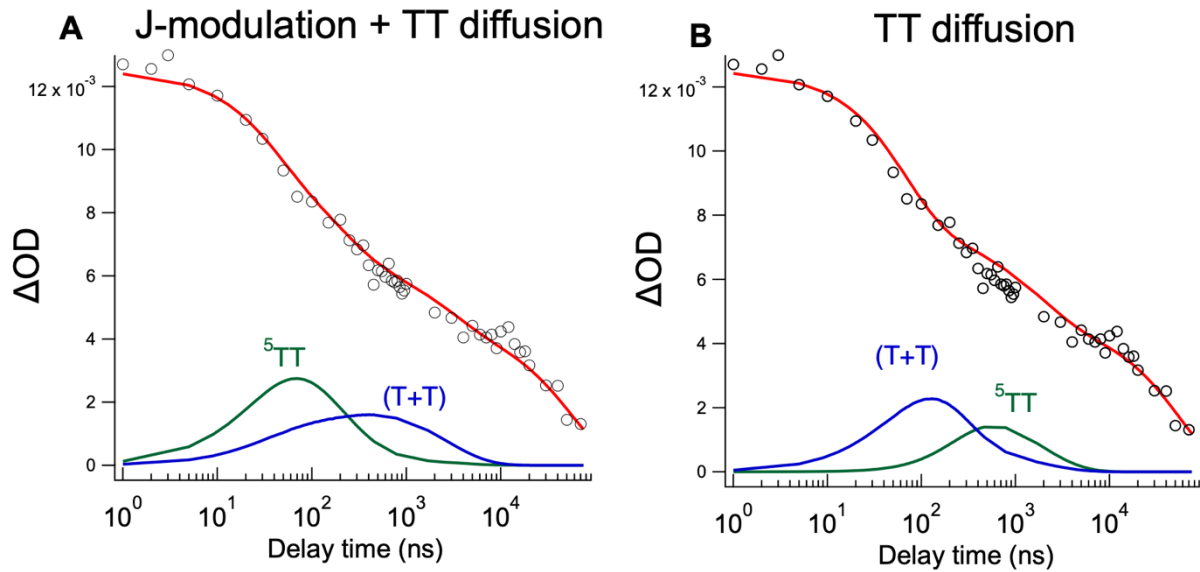


**Fig. S12. Computed ns-TA decay profiles using two different models at room temperature.** In (A), the red profile (Fig. 4C) is obtained with considering the  $J$ -modulation between  $J_1 = -1.4 \times 10^5$  MHz and  $J_2 = -1.9 \times 10^4$  MHz in  $TT_1$  and  $TT_2$ , respectively in Table S3. In (B),  $J_1 = J_2 = -1.4 \times 10^5$  MHz is set assuming that the  $J$  is frozen in the strongly coupled state. In this model (TT diffusion model), the TA decay profile is reproduced with  $k_{\text{DISS}} = 4.0 \times 10^6 \text{ s}^{-1}$ ,  $k_{\text{BACK}} = 4.0 \times 10^6 \text{ s}^{-1}$ , and  $k_{\text{REC}} = 2.4 \times 10^7 \text{ s}^{-1}$ . The green and blue profiles are contributions of the strongly coupled  ${}^5\text{TT}$  and the SCTP (T+T). In model A, the quick  ${}^5\text{TT}$  rise within 100 ns is consistent with the observation of the AAEEAE polarized quintet multiexciton at 100 ns in Fig. 4A. In model B, however, the contribution of the quintet state is minor at 100 ns and thus is inconsistent with the AAEEAE polarization at 100 ns.

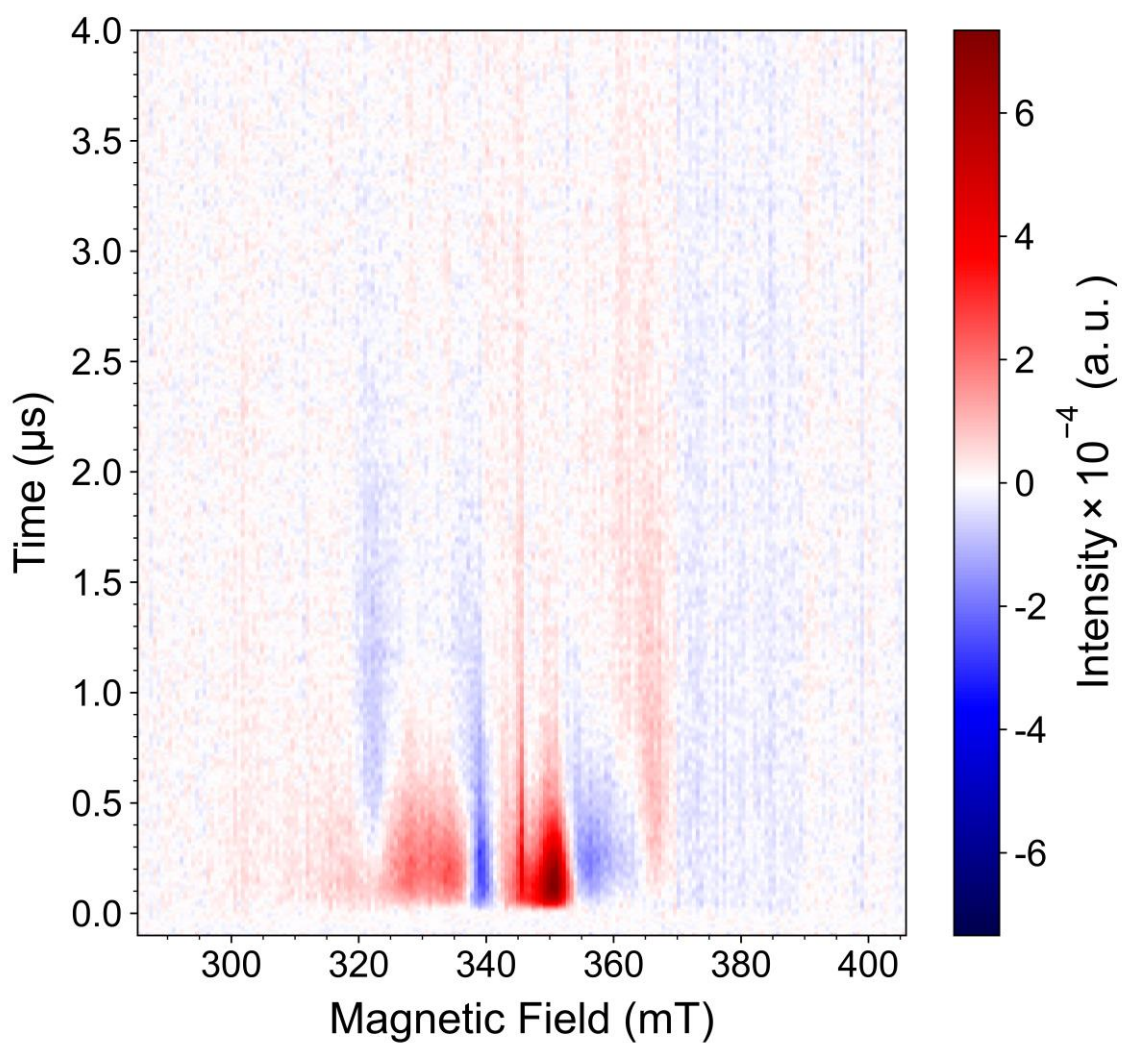


**Fig. S13.** 2D mapping of the TREPR data up to 4.0  $\mu\text{s}$  after laser irradiations obtained at room temperature in Fig. 4A.

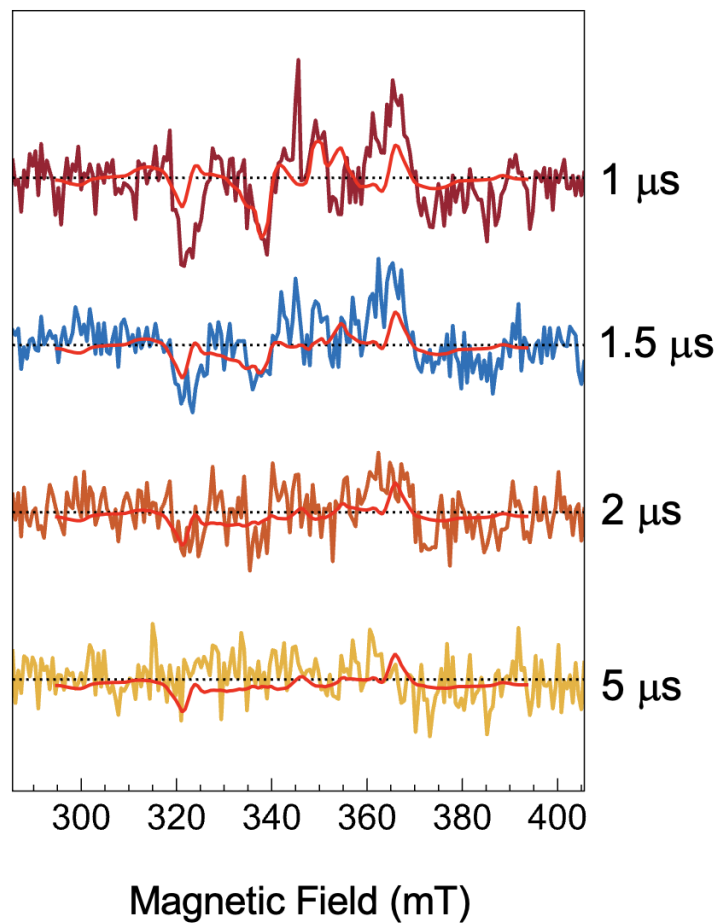


**Fig. S14.** Enlarged TREPR data for the delay times larger than 1  $\mu\text{s}$  in Fig. 4A.

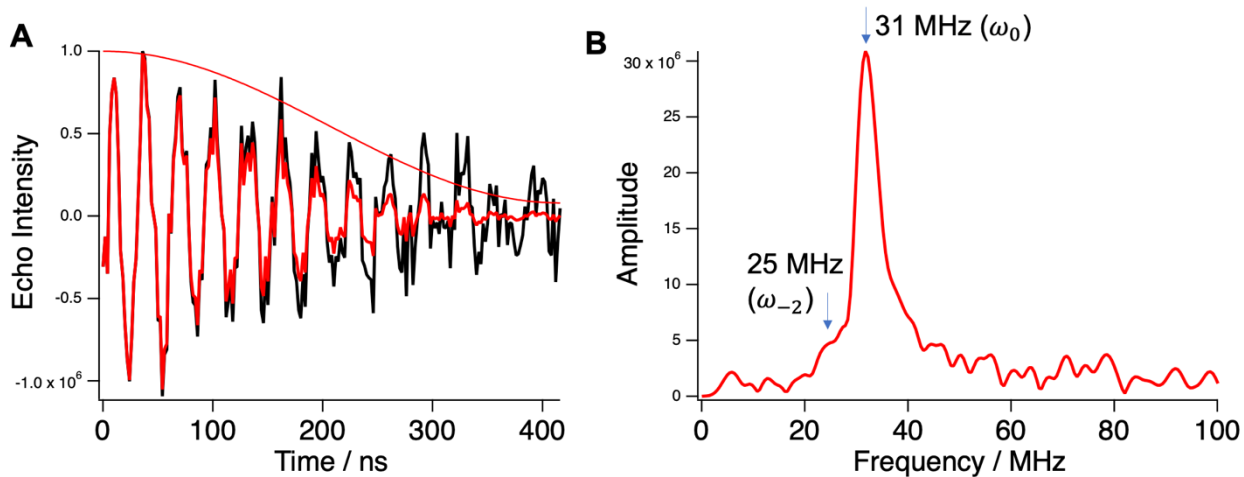


**Fig. S15. Nutation profile and nutation spectra in Fig. 6D.** (A) Nutation profile with introducing the window function shown by the red curve. (B) Fourier transform of the nutation data of the red line in (A), showing two different quintet nutation frequencies at 31 MHz and 25 MHz. Additional minor component is also obtained as a shoulder band at a higher frequency region around 37 MHz. This is due to the off-resonance effect caused by field directions nearby the  $Q_{0,1}$  region in Fig. S19. The width of the main peak is around 5 MHz and roughly coincides with  $2T_{2D} = 200$  ns together with the width of the minor peak at 25 MHz.

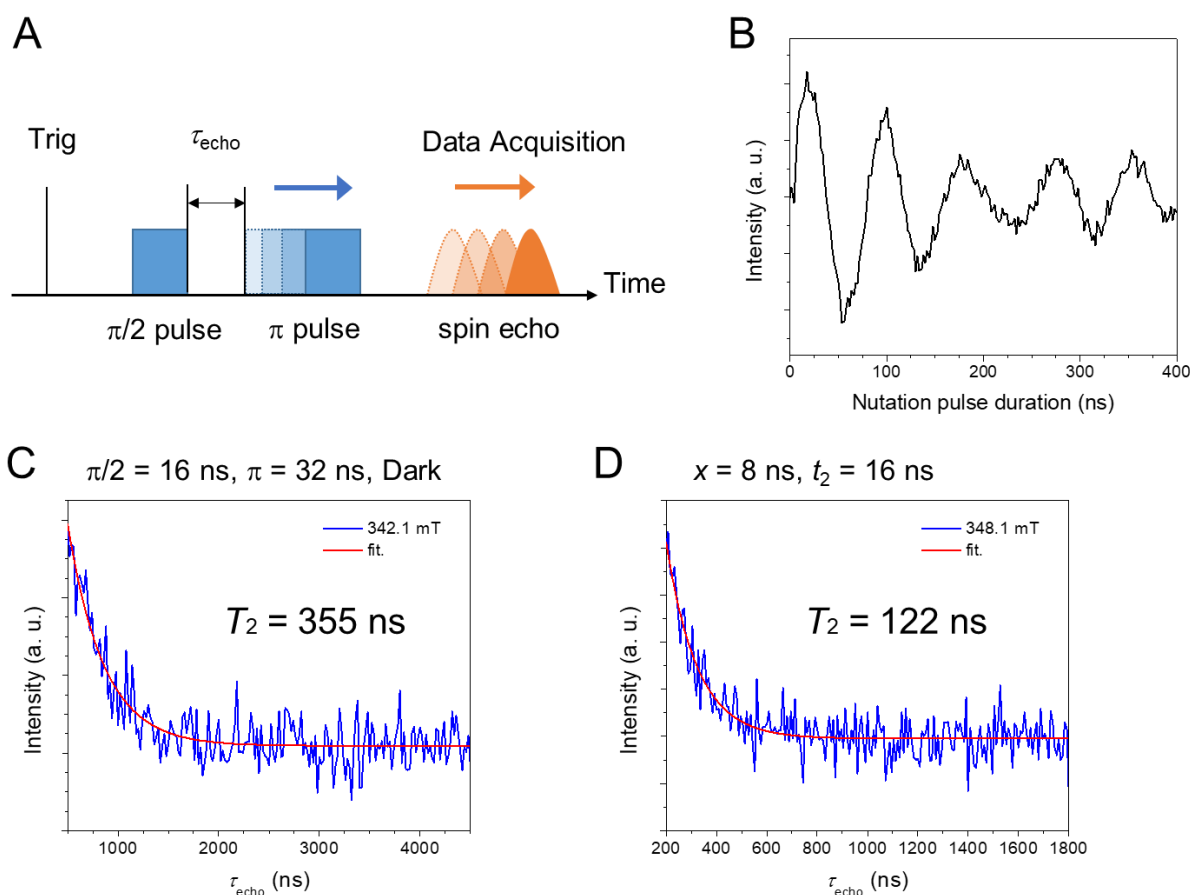


**Fig. S16. Coherence time of the radical species and the quintet triplet-pairs.** (A) Pulse sequence of the Hahn echo detection ( $\tau_{\text{delay}}-\pi/2-\tau_{\text{echo}}-\pi-\tau_{\text{echo}}-\text{echo}$ ) for isolated radical signal at  $B_0 = 342.10$  mT in the dark performed after the CWTREPR experiments. (B) The nutation profile of the radical species obtained by  $B_1 = 0.45$  mT at 342.10 mT with  $\pi = 32$  ns in the absence of the laser irradiation. The nutation frequency ( $= 12$  MHz) exhibits characteristic of the doublet frequency of  $g\mu_B B_1/\hbar$  by  $S = 1/2$  in eq. (4). (C) The transverse relaxation time of  $T_2 = 355$  ns was obtained by plotting the echo signal with varying  $\tau_{\text{echo}}$  in the radical species in the dark. (D) For the quintet triplet-pairs,  $T_2 = 122$  ns was obtained by plotting the echo signal with varying  $\tau_{\text{echo}}$  at  $B_0 = 348.10$  mT (blue arrow in Fig. 6C) with  $x = 8$  ns and  $t_2 = 16$  ns at  $\tau_{\text{echo}} = 1.1$   $\mu\text{s}$  in Fig. 6A.

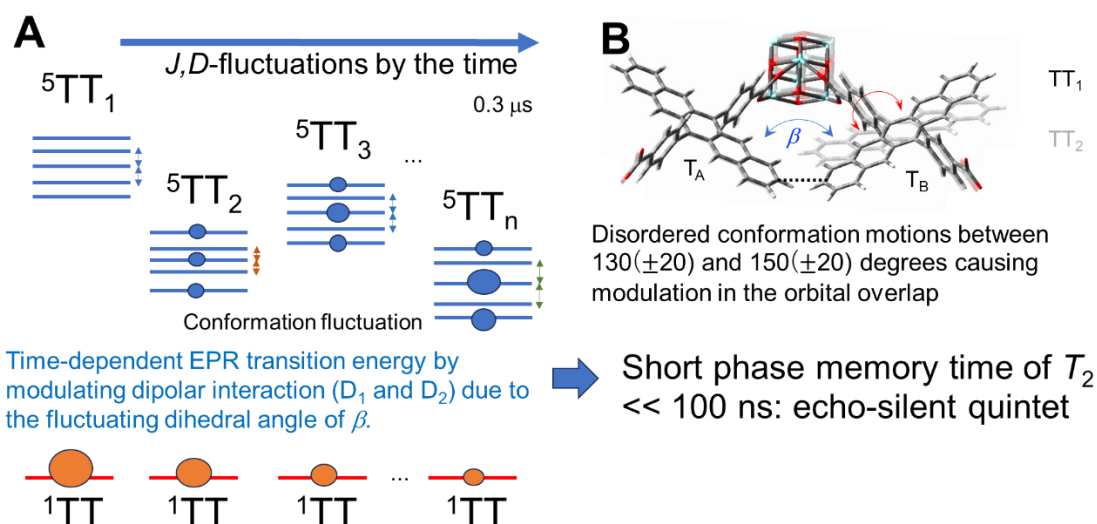


**Fig. S17. Schematic representations of time course of the singlet and quintet TT.** Schematic representations of (A) time course of the singlet and quintet TT at the disordered domain in the MOF after the singlet-fission and (B) the conformation dynamics. In (A), the quintet populations will be caused mainly by the modulation of the exchange coupling ( $6J$ ). The conformation dynamics can also induce the amplifications in the electronic coupling (orbital overlap in TT) for the quick singlet deactivation. Because the dipolar interaction in the  ${}^5\text{TT}$  is also time-dependent, the resonance magnetic field within the quintet sublevel is modulated, resulting in the major echo-silent EPR signal. This is highly distinguished from the species responsible for the echo generated at the minor ordered domain in the MOF sample.

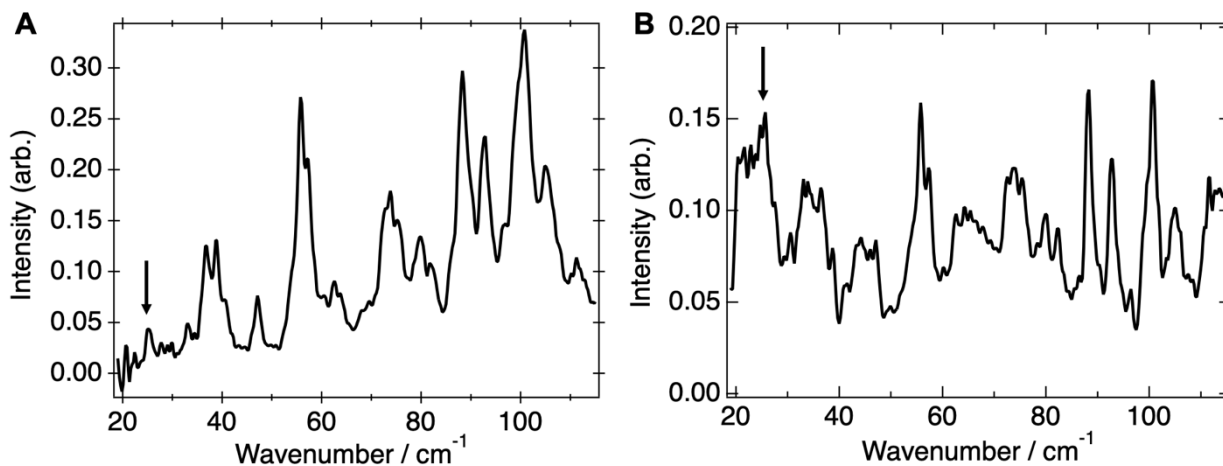


**Fig. S18. THz spectra of MOF.** THz spectra of Pn-MOF were measured using the THz-TDS spectrometer in a transmission set up in the air (A) and in paraffin (B) at room temperature. In (B), MOF in paraffin was measured in a polyethylene (PE) cell. In (A), the PE cell was not used for the powder sample. The arrows around  $25\text{ cm}^{-1}$  correspond to the frequency of the motion for the quintet generation in Fig. 6. There are several different motions in the solid sample. However, it is in principle important to note from the Redfield theory (49) that the singlet-quintet population relaxation is effectively caused when the energy gap by the negative  $J$ -coupling is close to the motion frequency in the solid. In addition,  $TT_2$  state needs to be thermally accessible for the spin conversion.

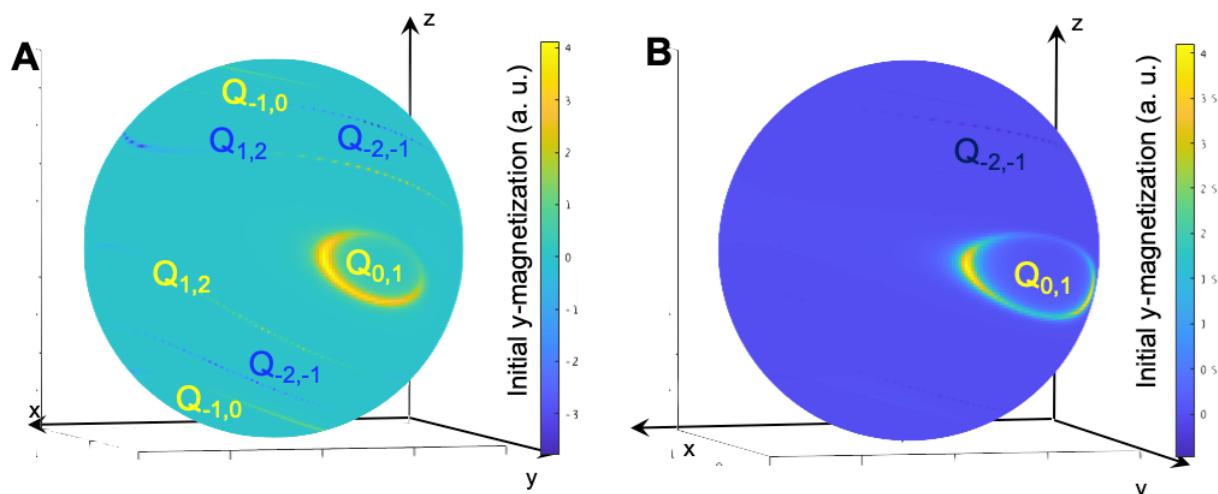


**Fig. S19. Angle selectivity of y-magnetization.** Angle selectivity of y-magnetization response for the field directions ( $B_0 = 348.1$  mT) created by the first microwave pulse in the quantum gates obtained from a powder-pattern calculation of the transient nutation profiles of the red solid and green dotted lines in Fig. 6E for **A**) and **B**), respectively. The positive magnetization represented by  $Q_{m_s, m_{s+1}}$  denotes overpopulation in the sublevel of  $m_s$  at the resonance transition between  $Q_{m_s}$  and  $Q_{m_{s+1}}$  with  $m_s = -2, -1, 0$  and  $1$ . These maps are obtained by plotting transverse magnetization responses (eq. S16) by the short first microwave pulse for the four different quantum gates to the magnetic field directions with respect to the molecular frame (x,y,z) of the principal axes of the zero-field splitting interaction of the  $T_A$  molecule. In **(A)**, the positive (yellowish) and negative (dark blue) magnetization regions by the  $Q_{0,1}$  gates (around the center of the sphere) and by the  $Q_{-1,0}$  gates (around the sphere poles) are obtained for the common nutation frequency of 31 MHz. Summation of these four components will result in the superposition of the amplitudes from the high and low frequency components in Fig. 6D, when the small degree of the molecular rotation is considered (Fig. 6). In **(B)**, the amplitude by the  $Q_{0,\pm 1}$  gates will be minor in the dashed line of Fig. 6E when the larger degree of motion is considered (Fig. 4B).

We were unable to discriminate the different transitions by the molecular orientations *experimentally*. Nevertheless, one can distribute the angle dependence of the y-magnetizations to the space directions from the powder pattern analysis of the nutation profile (Fig. 6D) and of the echo-detected EPR spectrum (Fig. 6C), as shown in (A). From this, it is reasonably assigned that the quantum gate at  $B_0 = 348.1$  mT (See arrow at Fig. 6C) is dominated by the  $Q_0$ - $Q_1$  transition, meaning that the specific transition can be selected simply by the external magnetic field position. Therefore, the major and minor transitions are selected by the magnetic field due to the large anisotropic effect by the dipolar interaction.

**Table S1.** Matrix elements of  $L$  in  $\partial\vec{\rho}/\partial t = L\rho$  described in the basis spin system of  $\hat{H}_{\text{TT1}}$  utilized for  $m_S = \pm 2$  mixed with singlet states.<sup>a)</sup>

$\rho_{\text{QQ1}}$	$-k_{12}$ $-k_{\text{DISS}}$			$k_{21}$				$k_{\text{Back}}$			
$\rho_{\text{QS1}}$	$-k_{12}-k_{\text{DISS}}-$ $k_{\text{REC}}/2-i(\$ $E_{\text{Qms}}^{\text{TT1}}-E_{\text{S}}^{\text{TT1}})$			$k_{21}$				$k_{\text{Back}}$			
$\rho_{\text{SQ1}}$		$-k_{12}-k_{\text{DISS}}$ $-k_{\text{REC}}/2+i$ $(E_{\text{Qms}}^{\text{TT1}}-$ $E_{\text{S}}^{\text{TT1}})$			$k_{21}$					$k_{\text{Back}}$	
$\rho_{\text{SS1}}$			$-k_{12}$ $-k_{\text{DISS}}-k_{\text{R}}$ EC				$k_{21}$				$k_{\text{Back}}$
$\rho_{\text{QQ2}}$	$k_{12}$			$-k_{21}$	$iH_{\text{SQms}}^{\text{TT2}}$	$-iH_{\text{QmsS}}^{\text{TT2}}$					
$\rho_{\text{QS2}}$	$k_{12}$			$iH_{\text{QmsS}}^{\text{TT2}}$	$-i(H_{\text{QmsQms}}^{\text{TT2}}$ $-H_{\text{SS}}^{\text{TT2}})-k_{21}$		$-iH_{\text{QmsS}}^{\text{TT2}}$				
$\rho_{\text{SQ2}}$		$k_{12}$		$-iH_{\text{SQms}}^{\text{TT2}}$		$i(H_{\text{QmsQms}}^{\text{TT2}}-$ $H_{\text{SS}}^{\text{TT2}})-k_{21}$	$iH_{\text{SQms}}^{\text{TT2}}$				
$\rho_{\text{SS2}}$			$k_{12}$		$-iH_{\text{SQms}}^{\text{TT2}}$	$iH_{\text{QmsS}}^{\text{TT2}}$	$-k_{21}$				
$\rho_{\text{QQ(T+T)}}$	$k_{\text{DISS}}$							$-k_{\text{Back}}$	$iH_{\text{SQms}}^{\text{T+T}}$	$-iH_{\text{QmsS}}^{\text{T+T}}$	
$\rho_{\text{QS(T+T)}}$	$k_{\text{DISS}}$							$iH_{\text{QmsS}}^{\text{T+T}}$	$-i(H_{\text{QmsQms}}^{\text{T+T}}$ $-H_{\text{SS}}^{\text{T+T}})-k_{\text{S}}/$ $2-k_{\text{Back}}$		$-iH_{\text{QmsS}}^{\text{T+T}}$
$\rho_{\text{SQ(T+T)}}$		$k_{\text{DISS}}$						$-iH_{\text{SQms}}^{\text{T+T}}$		$i(H_{\text{QmsQms}}^{\text{T+T}}-$ $H_{\text{SS}}^{\text{T+T}})-$ $k_{\text{S}}/2-k_{\text{Back}}$	$iH_{\text{SQms}}^{\text{T+T}}$
$\rho_{\text{SS(T+T)}}$			$k_{\text{DISS}}$						$-iH_{\text{SQms}}^{\text{T+T}}$	$iH_{\text{QmsS}}^{\text{T+T}}$	$-k_{\text{S}}-k_{\text{Back}}$

<sup>a)</sup> We chose the basis set obtained by diagonalizing the spin Hamiltonian of  $\hat{H}_{\text{TT1}}$ . The matrix identified by the bold frame is replaced by Table S2 for  $m_S = \pm 1$  and  $m_S = 0$  coupled with  $m = \pm 1$  and  $m = 0$ , respectively.

**Table S2.** Matrix elements of  $L$  in  $\partial\vec{p}/\partial t = L\rho$  described for the T+T states when  $m_S = \pm 1$  ( $m_S = 0$ ) are mixed with  $m = \pm 1$  ( $m = 0$ ), respectively, together with the singlet T+T state. Q and T denote  $Q_{m_S}$  and  $T_m$  of the T+T multiexciton, respectively.

T+T	QQ	QT	QS	TQ	TT	TS	SQ	ST	SS
QQ	$-k_{\text{Back}}$	$iH_{\text{TQ}}$	$iH_{\text{SQ}}$	$-iH_{\text{QT}}$			$-iH_{\text{QS}}$		
QT	$iH_{\text{QT}}$	$-i(H_{\text{QQ}} - H_{\text{TT}}) - k_{\text{Back}} - k_{\text{T}}/2$	$iH_{\text{ST}}$		$-iH_{\text{QT}}$			$-iH_{\text{QS}}$	
QS	$iH_{\text{QS}}$	$iH_{\text{TS}}$	$-i(H_{\text{QQ}} - H_{\text{SS}}) - k_{\text{Back}} - k_{\text{S}}/2$			$-iH_{\text{QT}}$			$-iH_{\text{QS}}$
TQ	$-iH_{\text{TQ}}$			$-i(H_{\text{TT}} - H_{\text{QQ}}) - k_{\text{Back}} - k_{\text{T}}/2$	$iH_{\text{TQ}}$	$iH_{\text{SQ}}$	$-iH_{\text{TS}}$		
TT		$-iH_{\text{TQ}}$		$iH_{\text{QT}}$	$-k_{\text{Back}} - k_{\text{T}}$	$iH_{\text{ST}}$		$-iH_{\text{TS}}$	
TS			$-iH_{\text{TQ}}$	$iH_{\text{QS}}$	$iH_{\text{TS}}$	$-i(H_{\text{TT}} - H_{\text{SS}}) - k_{\text{Back}} - k_{\text{T}}/2 - k_{\text{S}}/2$			$-iH_{\text{TS}}$
SQ	$-iH_{\text{SQ}}$			$-iH_{\text{ST}}$			$-i(H_{\text{SS}} - H_{\text{QQ}}) - k_{\text{Back}} - k_{\text{S}}/2$	$iH_{\text{TQ}}$	$iH_{\text{SQ}}$
ST		$-iH_{\text{SQ}}$			$-iH_{\text{ST}}$		$iH_{\text{QT}}$	$-i(H_{\text{SS}} - H_{\text{TT}}) - k_{\text{Back}} - k_{\text{T}}/2 - k_{\text{S}}/2$	$iH_{\text{ST}}$
SS			$-iH_{\text{SQ}}$			$-iH_{\text{ST}}$	$iH_{\text{QS}}$	$iH_{\text{TS}}$	$-k_{\text{Back}} - k_{\text{S}}$

**Table S3.** Parameters for computations of the delay time dependence of the EPR spectra and absorbance changes in paraffin, considering the conformation motions between TT<sub>1</sub> and TT<sub>2</sub> states by the multiexciton motions with the frequency of  $\bar{\nu}_{\text{vib}}$  in the model of Fig. 5. (20, 51)

		$J/\text{MHz}$	$D/\text{MHz}$ a)	$E/\text{MHz}$ <sup>a)</sup>	$D_{\text{SS}}/\text{MHz}$	Euler angles <sup>b)</sup> / degrees ( $\alpha, \beta, \gamma$ )	Polar angles <sup>c)</sup> degrees	$\bar{\nu}_{\text{vib}}/\text{cm}^{-1}$	$\Delta E_{12}/\text{cm}^{-1}$ d)	$k_{\text{Diss}}^{\text{e)}/\text{s}^{-1}}$	$k_{\text{Rec}}^{\text{e)}/\text{s}^{-1}}$
150 K	TT <sub>1</sub>	$-1.4 \times 10^5$	1,225	-20	-95	$\alpha = 95$ $\beta = 164$ $\gamma = -30$	$\theta_2 = 70$ $\phi_2 = 160$	15	30	$8.0 \times 10^5$ ( $1.2 \times 10^6$ )	$1.6 \times 10^7$ ( $2.0 \times 10^7$ )
	TT <sub>2</sub>	$-1.9 \times 10^4$	1,164	-20	-95	$\alpha = 90$ $\beta = 113$ $\gamma = 0$	$\theta_2 = 70$ $\phi_2 = 160$			-	
	T+T	28	1,225	-20	-45	$\alpha = 0$ $\beta = 125$ $\gamma = 0$	$\theta_2 = 101$ $\phi_2 = 210$	-	-	$2.3 \times 10^5$ ( $2.8 \times 10^5$ )	-
300 K	TT <sub>1</sub>	$-1.4 \times 10^5$	1,200	-20	-105	$\alpha = 90$ $\beta = 130$ $\gamma = -20$	$\theta_2 = 70$ $\phi_2 = 160$	14	30	$3.0 \times 10^6$ ( $3.0 \times 10^6$ )	$5.6 \times 10^7$ ( $5.6 \times 10^7$ )
	TT <sub>2</sub>	$-1.9 \times 10^4$	1,140	-20	-105	$\alpha = 90$ $\beta = 150$ $\gamma = -40$	$\theta_2 = 70$ $\phi_2 = 160$			-	
	T+T	28	1,200	-20	-45	$\alpha = 0$ $\beta = 125$ $\gamma = 0$	$\theta_2 = 101$ $\phi_2 = 210$	-	-	$1.1 \times 10^6$ ( $1.1 \times 10^6$ )	-

a) Zero-field splitting parameters in  $\mathbf{H}_{\text{zfs}} = D\{S_z^2 - S(S+1)/3\} + E(S_x^2 - S_y^2)$  for each triplet in the T<sub>A</sub>T<sub>B</sub> multiexciton.

b) Conformation of the principal axes in  $\mathbf{H}_{\text{zfs}}$  of the T<sub>B</sub> component with respect to the principal axes of T<sub>A</sub> component in the T<sub>A</sub>T<sub>B</sub> multiexciton with the x-convention.

c) Direction for the T<sub>B</sub> component was set by the polar angles ( $\theta_2$  and  $\phi_2$ ) with respect the (X<sub>1</sub>, Y<sub>1</sub>, Z<sub>1</sub>) principal axes in T<sub>A</sub>.

d) The energy gap between TT<sub>1</sub> and TT<sub>2</sub> states represented by  $\Delta E_{12} = E(\text{TT}_2) - E(\text{TT}_1)$ .

e) The kinetic parameters are shown in the parentheses to fit the transient absorbance changes (Fig. 3) of the triplet excitons in the absence of the external magnetic field by the present vibronic model analysis.

**Table S4.** Parameters for computations of the delay time dependence of the EPR spectra in paraffin in Figure S10B, considering the conformation motions between TT<sub>1</sub> and TT<sub>2</sub> states. (20, 51)

		$J$ /MHz	$D$ /MHz	$E$ /MHz	$D_{ss}$ /MHz	Euler angles / degrees ( $\alpha, \beta, \gamma$ )	Polar angles / degrees	$\bar{\nu}_{vib}$ / cm <sup>-1</sup>	$\Delta E_{12}$ / cm <sup>-1</sup>	$k_{Diss}$ / s <sup>-1</sup>	$k_{Rec}$ / s <sup>-1</sup>
										$k_{Back}$ / s <sup>-1</sup>	
300 K	TT <sub>1</sub>	$-1.7 \times 10^5$	1,200	-20	-45	$\alpha = 90$ $\beta = 125$ $\gamma = -30$	$\theta_2 = 40$ $\phi_2 = 160$	1.9	30	$3.0 \times 10^6$	$5.6 \times 10^7$
	TT <sub>2</sub>	$-2.2 \times 10^4$	1,140	-20	-45	$\alpha = 90$ $\beta = 110$ $\gamma = -40$	$\theta_2 = 40$ $\phi_2 = 160$				-
	T+T	28	1,200	-20	-45	$\alpha = 0$ $\beta = 125$ $\gamma = 0$	$\theta_2 = 101$ $\phi_2 = 210$	-	-	$1.1 \times 10^6$	-

**Table S5.** Parameters for computations of the transient nutation and delay time dependence of echo signal at  $B_0 = 348.1$  mT at 300 K ( $\tau_{delay} = 1.1$   $\mu$ s), considering the conformation motions between TT<sub>1</sub> and TT<sub>2</sub> states for computations of the sublevel populations ( $\rho_{m_S m_S}^{TT1}$  and  $\rho_{m_S m_S}^{TT2}$ ) and the sublevel energies ( $E_{Q_{m_S}}^{TT1}$  and  $E_{Q_{m_S}}^{TT2}$ ) in eq. (S3) by the multiexciton motions with the frequency of  $\bar{\nu}_{vib}$  in the model of Fig. 5 (20, 51).

		$J$ /MHz	$D$ /MHz	$E$ /MHz	$D_{ss}$ /MHz	Euler angles / degrees ( $\alpha, \beta, \gamma$ )	Polar angles / degrees	$\bar{\nu}_{vib}$ / cm <sup>-1</sup>	$\Delta E_{12}$ / cm <sup>-1</sup>	$k_{Diss}$ / s <sup>-1</sup> a)	$k_{Rec}$ / s <sup>-1</sup>
										$k_{Back}$ / s <sup>-1</sup> a)	
300 K	TT <sub>1</sub>	$-1.7 \times 10^5$	1,225	-25	-105	$\alpha = 90$ $\beta = 130$ $\gamma = -20$	$\theta_2 = 70$ $\phi_2 = 160$	22	20	$< 10^3$	$1.5 \times 10^6$
	TT <sub>2</sub>	$-2.2 \times 10^4$	1,164	-25	-105	$\alpha = 90$ $\beta = 122$ $\gamma = -30$	$\theta_2 = 70$ $\phi_2 = 160$				-
	T+T <sup>a)</sup>	-	-	-	-	-	-	-	-	-	$< 10^3$

<sup>a)</sup> T+T dissociation is not considered ( $k_{Diss} < 10^3$  s<sup>-1</sup>) in the trap multiexciton.

## REFERENCES AND NOTES

1. F. Arute, K. Arya, R. Babbush, D. Bacon, J. C. Bardin, R. Barends, R. Biswas, S. Boixo, F. Brandao, D. A. Buell, B. Burkett, Y. Chen, Z. Chen, B. Chiaro, R. Collins, W. Courtney, A. Dunsworth, E. Farhi, B. Foxen, A. Fowler, C. Gidney, M. Giustina, R. Graff, K. Guerin, S. Habegger, M. P. Harrigan, M. J. Hartmann, A. Ho, M. Hoffmann, T. Huang, T. S. Humble, S. V. Isakov, E. Jeffrey, Z. Jiang, D. Kafri, K. Kechedzhi, J. Kelly, P. V. Klimov, S. Knysh, A. Korotkov, F. Kostritsa, D. Landhuis, M. Lindmark, E. Lucero, D. Lyakh, S. Mandra, J. R. McClean, M. McEwen, A. Megrant, X. Mi, K. Michielsen, M. Mohseni, J. Mutus, O. Naaman, M. Neeley, C. Neill, M. Y. Niu, E. Ostby, A. Petukhov, J. C. Platt, C. Quintana, E. G. Rieffel, P. Roushan, N. C. Rubin, D. Sank, K. J. Satzinger, V. Smelyanskiy, K. J. Sung, M. D. Trevithick, A. Vainsencher, B. Villalonga, T. White, Z. J. Yao, P. Yeh, A. Zalcman, H. Neven, J. M. Martinis, Quantum supremacy using a programmable superconducting processor. *Nature* **574**, 505–510 (2019).
2. T. D. Ladd, F. Jelezko, R. Laflamme, Y. Nakamura, C. Monroe, J. L. O'Brien, Quantum computers. *Nature* **464**, 45–53 (2010).
3. M. K. Bhaskar, R. Riedinger, B. Machielse, D. S. Levonian, C. T. Nguyen, E. N. Knall, H. Park, D. Englund, M. Loncar, D. D. Sukachev, M. D. Lukin, Experimental demonstration of memory-enhanced quantum communication. *Nature* **580**, 60–64 (2020).
4. S. Muralidharan, L. Li, J. Kim, N. Lutkenhaus, M. D. Lukin, L. Jiang, Optimal architectures for long distance quantum communication. *Sci. Rep.* **6**, 20463 (2016).
5. C. L. Degen, F. Reinhard, P. Cappellaro, Quantum sensing. *Rev. Mod. Phys.* **89**, 035002 (2017).
6. X. Guo, C. R. Breum, J. Borregaard, S. Izumi, M. V. Larsen, T. Gehring, M. Christandl, J. S. Neergaard-Nielsen, U. L. Andersen, Distributed quantum sensing in a continuous-variable entangled network. *Nat. Phys.* **16**, 281–284 (2019).
7. J. R. Maze, P. L. Stanwix, J. S. Hodges, S. Hong, J. M. Taylor, P. Cappellaro, L. Jiang, M. V. Dutt, E. Togan, A. S. Zibrov, A. Yacoby, R. L. Walsworth, M. D. Lukin, Nanoscale magnetic sensing with an individual electronic spin in diamond. *Nature* **455**, 644–647 (2008).
8. J. M. Zadrozny, A. T. Gallagher, T. D. Harris, D. E. Freedman, A porous array of clock qubits. *J. Am. Chem. Soc.* **139**, 7089–7094 (2017).

9. S. von Kugelgen, M. D. Krzyaniak, M. Gu, D. Puggioni, J. M. Rondinelli, M. R. Wasielewski, D. E. Freedman, Spectral addressability in a modular two qubit system. *J. Am. Chem. Soc.* **143**, 8069–8077 (2021).
10. M. R. Wasielewski, M. D. E. Forbes, N. L. Frank, K. Kowalski, G. D. Scholes, J. Yuen-Zhou, M. A. Baldo, D. E. Freedman, R. H. Goldsmith, T. Goodson, M. L. Kirk, J. K. McCusker, J. P. Ogilvie, D. A. Shultz, S. Stoll, K. B. Whaley, Exploiting chemistry and molecular systems for quantum information science. *Nat. Rev. Chem.* **4**, 490–504 (2020).
11. S. L. Bayliss, D. W. Laorenza, P. J. Mintun, B. D. Kovos, D. E. Freedman, D. D. Awschalom, Optically addressable molecular spins for quantum information processing. *Science* **370**, 1309–1312 (2020).
12. Y. Qiu, A. Equbal, C. Lin, Y. Huang, P. J. Brown, R. M. Young, M. D. Krzyaniak, M. R. Wasielewski, Optical spin polarization of a narrow-linewidth electron-spin qubit in a chromophore/stable-radical system. *Angew. Chem. Int. Ed. Engl.* **62**, e202214668 (2023).
13. L. R. Weiss, S. L. Bayliss, F. Kraffert, K. J. Thorley, J. E. Anthony, R. Bittl, R. H. Friend, A. Rao, N. C. Greenham, J. Behrends, Strongly exchange-coupled triplet pairs in an organic semiconductor. *Nat. Phys.* **13**, 176–181 (2016).
14. R. D. Dill, K. E. Smyser, B. K. Rugg, N. H. Damrauer, J. D. Eaves, Entangled spin-polarized excitons from singlet fission in a rigid dimer. *Nat. Commun.* **14**, 1180 (2023).
15. R. M. Jacobberger, Y. Qiu, M. L. Williams, M. D. Krzyaniak, M. R. Wasielewski, Using molecular design to enhance the coherence time of quintet multiexcitons generated by singlet fission in single crystals. *J. Am. Chem. Soc.* **144**, 2276–2283 (2022).
16. H. Nagashima, S. Kawaoka, S. Akimoto, T. Tachikawa, Y. Matsui, H. Ikeda, Y. Kobori, Singlet-fission-born quintet state: Sublevel selections and trapping by multiexciton thermodynamics. *J. Phys. Chem. Lett.* **9**, 5855–5861 (2018).
17. S. L. Bayliss, L. R. Weiss, F. Kraffert, D. B. Granger, J. E. Anthony, J. Behrends, R. Bittl, Probing the wave function and dynamics of the quintet multiexciton state with coherent control in a singlet fission material. *Phys. Rev. X* **10**, 021070 (2020).
18. D. Lubert-Perquel, E. Salvadori, M. Dyson, P. N. Stavrinou, R. Montis, H. Nagashima, Y. Kobori, S. Heutz, C. W. M. Kay, Identifying triplet pathways in dilute pentacene films. *Nat. Commun.* **9**, 4222 (2018).

19. T. S. C. MacDonald, M. J. Y. T. M. I. Collins, E. Kumarasamy, S. N. S. M. Y. Sfeir, L. M. Campos, D. R. McCamey, Anisotropic multiexciton quintet and triplet dynamics in singlet fission via pulsed electron spin resonance. *J. Am. Chem. Soc.* **145**, 15275–15283 (2023).
20. Y. Kobori, M. Fuki, S. Nakamura, T. Hasobe, Geometries and terahertz motions driving quintet multiexcitons and ultimate triplet-triplet dissociations via the intramolecular singlet fissions. *J. Phys. Chem. B* **124**, 9411–9419 (2020).
21. K. E. Smyser, J. D. Eaves, Singlet fission for quantum information and quantum computing: The parallel JDE model. *Sci. Rep.* **10**, 18480 (2020).
22. M. I. Collins, D. R. McCamey, M. J. Y. Tayebjee, Fluctuating exchange interactions enable quintet multiexciton formation in singlet fission. *J. Chem. Phys.* **151**, 164104 (2019).
23. S. Matsuda, S. Oyama, Y. Kobori, Electron spin polarization generated by transport of singlet and quintet multiexcitons to spin-correlated triplet pairs during singlet fissions. *Chem. Sci.* **11**, 2934–2942 (2020).
24. P. J. Budden, L. R. Weiss, M. Muller, N. A. Panjwani, S. Dowland, J. R. Allardice, M. Ganschow, J. Freudenberg, J. Behrends, U. H. F. Bunz, R. H. Friend, Singlet exciton fission in a modified acene with improved stability and high photoluminescence yield. *Nat. Commun.* **12**, 1527 (2021).
25. S. R. E. Orsborne, J. Gorman, L. R. Weiss, A. Sridhar, N. A. Panjwani, G. Divitini, P. Budden, D. Palecek, S. T. J. Ryan, A. Rao, R. Colleparado-Guevara, A. H. El-Sagheer, T. Brown, J. Behrends, R. H. Friend, F. Auras, Photogeneration of spin quintet triplet-triplet excitations in DNA-assembled pentacene stacks. *J. Am. Chem. Soc.* **145**, 5431–5438 (2023).
26. M. I. Collins, F. Campaioli, M. J. Y. Tayebjee, J. H. Cole, D. R. McCamey, Quintet formation, exchange fluctuations, and the role of stochastic resonance in singlet fission. *Commun. Phys.* **6**, 64 (2023).
27. M. Einzinger, T. Wu, J. F. Kompalla, H. L. Smith, C. F. Perkinson, L. Nienhaus, S. Wieghold, D. N. Congreve, A. Kahn, M. G. Bawendi, M. A. Baldo, Sensitization of silicon by singlet exciton fission in tetracene. *Nature* **571**, 90–94 (2019).
28. K. Miyata, F. S. Conrad-Burton, F. L. Geyer, X. Y. Zhu, Triplet pair states in singlet fission. *Chem. Rev.* **119**, 4261–4292 (2019).
29. M. B. Smith, J. Michl, Singlet fission. *Chem. Rev.* **110**, 6891–6936 (2010).

30. S. Kitagawa, R. Kitaura, S. Noro, Functional porous coordination polymers. *Angew. Chem. Int. Ed. Engl.* **43**, 2334–2375 (2004).
31. M. C. So, G. P. Wiederrecht, J. E. Mondloch, J. T. Hupp, O. K. Farha, Metal-organic framework materials for light-harvesting and energy transfer. *Chem. Commun.* **51**, 3501–3510 (2015).
32. B. Joarder, A. Mallick, Y. Sasaki, M. Kinoshita, R. Haruki, Y. Kawashima, N. Yanai, N. Kimizuka, Near-infrared-to-visible photon upconversion by introducing an S–T absorption sensitizer into a metal-organic framework. *ChemNanoMat* **6**, 916–919 (2020).
33. R. Haldar, M. Kozłowska, M. Ganschow, S. Ghosh, M. Jakoby, H. Chen, F. Ghalami, W. Xie, S. Heidrich, Y. Tsutsui, J. Freudenberg, S. Seki, I. A. Howard, B. S. Richards, U. H. F. Bunz, M. Elstner, W. Wenzel, C. Woll, Interplay of structural dynamics and electronic effects in an engineered assembly of pentacene in a metal-organic framework. *Chem. Sci.* **12**, 4477–4483 (2021).
34. S. Fujiwara, N. Matsumoto, K. Nishimura, N. Kimizuka, K. Tateishi, T. Uesaka, N. Yanai, Triplet dynamic nuclear polarization of guest molecules through induced fit in a flexible metal-organic framework. *Angew. Chem. Int. Ed. Engl.* **61**, e202115792 (2022).
35. O. M. Yaghi, M. O’Keeffe, N. W. Ockwig, H. K. Chae, M. Eddaoudi, J. Kim, Reticular synthesis and the design of new materials. *Nature* **423**, 705–714 (2003).
36. S. Fujiwara, M. Hosoyamada, K. Tateishi, T. Uesaka, K. Ideta, N. Kimizuka, N. Yanai, Dynamic nuclear polarization of metal-organic frameworks using photoexcited triplet electrons. *J. Am. Chem. Soc.* **140**, 15606–15610 (2018).
37. J. H. Cavka, S. Jakobsen, U. Olsbye, N. Guillou, C. Lamberti, S. Bordiga, K. P. Lillerud, A new zirconium inorganic building brick forming metal organic frameworks with exceptional stability. *J. Am. Chem. Soc.* **130**, 13850–13851 (2008).
38. H. Sakai, R. Inaya, H. Nagashima, S. Nakamura, Y. Kobori, N. V. Tkachenko, T. Hasobe, Multiexciton dynamics depending on intramolecular orientations in pentacene dimers: Recombination and dissociation of correlated triplet pairs. *J. Phys. Chem. Lett.* **9**, 3354–3360 (2018).
39. S. N. Sanders, E. Kumarasamy, A. B. Pun, M. T. Trinh, B. Choi, J. Xia, E. J. Taffet, J. Z. Low, J. R. Miller, X. Roy, X. Y. Zhu, M. L. Steigerwald, M. Y. Sfeir, L. M. Campos,

- Quantitative intramolecular singlet fission in bipentacenes. *J. Am. Chem. Soc.* **137**, 8965–8972 (2015).
40. B. J. Walker, A. J. Musser, D. Beljonne, R. H. Friend, Singlet exciton fission in solution. *Nat. Chem.* **5**, 1019–1024 (2013).
41. Y. Kawashima, T. Hamachi, A. Yamauchi, K. Nishimura, Y. Nakashima, S. Fujiwara, N. Kimizuka, T. Ryu, T. Tamura, M. Saigo, K. Onda, S. Sato, Y. Kobori, K. Tateishi, T. Uesaka, G. Watanabe, K. Miyata, N. Yanai, Singlet fission as a polarized spin generator for dynamic nuclear polarization. *Nat. Commun.* **14**, 1056 (2023).
42. Y. Y. Pan, J. Huang, Z. M. Wang, D. W. Yu, B. Yang, Y. G. Ma, Computational investigation on the large energy gap between the triplet excited-states in acenes. *RSC Adv.* **7**, 26697–26703 (2017).
43. J. Perego, C. X. Bezuidenhout, I. Villa, F. Cova, R. Crapanzano, I. Frank, F. Pagano, N. Kratochwill, E. Auffray, S. Bracco, A. Vedda, C. Dujardin, P. E. Sozzani, F. Meinardi, A. Comotti, A. Monguzzi, Highly luminescent scintillating hetero-ligand MOF nanocrystals with engineered stokes shift for photonic applications. *Nat. Commun.* **13**, 3504 (2022).
44. M. A. Ali, J. Ren, T. Zhao, X. Liu, Y. Hua, Y. Yue, J. Qiu, Broad mid-infrared luminescence in a metal-organic framework glass. *ACS Omega* **4**, 12081–12087 (2019).
45. A. J. Musser, M. Liebel, C. Schnedermann, T. Wende, T. B. Kehoe, A. Rao, P. Kukura, Evidence for conical intersection dynamics mediating ultrafast singlet exciton fission. *Nat. Phys.* **11**, 352–357 (2015).
46. P. A. Banks, E. M. Kleist, M. T. Ruggiero, Investigating the function and design of molecular materials through terahertz vibrational spectroscopy. *Nat. Rev. Chem.* **7**, 480–495 (2023).
47. S. L. Bayliss, L. R. Weiss, A. Mitioglu, K. Galkowski, Z. Yang, K. Yunusova, A. Surrente, K. J. Thorley, J. Behrends, R. Bittl, J. E. Anthony, A. Rao, R. H. Friend, P. Plochocka, P. C. M. Christianen, N. C. Greenham, A. D. Chepelianskii, Site-selective measurement of coupled spin pairs in an organic semiconductor. *Proc. Natl. Acad. Sci. U.S.A.* **115**, 5077–5082 (2018).
48. T. Yago, K. Ishikawa, R. Katoh, M. Wakasa, Magnetic field effects on triplet pair generated by singlet fission in an organic crystal: Application of radical pair model to triplet pair. *J. Phys. Chem. C* **120**, 27858–27870 (2016).

49. Y. Matsui, S. Kawaoka, H. Nagashima, T. Nakagawa, N. Okamura, T. Ogaki, E. Ohta, S. Akimoto, A. Sato-Tomita, S. Yagi, Y. Kobori, H. Ikeda, Exergonic intramolecular singlet fission of an adamantane-linked tetracene dyad via twin quintet multiexcitons. *J. Phys. Chem. C* **123**, 18813–18823 (2019).
50. Accelrys, Material Studio Release Notes, Release 4.2 (Accelrys Software, San Diego, 2006).
51. S. Nakamura, H. Sakai, H. Nagashima, M. Fuki, K. Onishi, R. Khan, Y. Kobori, N. V. Tkachenko, T. Hasobe, Synergetic role of conformational flexibility and electronic coupling for quantitative intramolecular singlet fission. *J. Phys. Chem. C* **125**, 18287–18296 (2021).
52. M. Gierer, A. v. d. Est, D. Stehlik, Transient EPR of weakly coupled spin-correlated radical pairs in photosynthetic reaction centres: Increase spectral resolution from nutation analysis. *Chem. Phys. Lett.* **186**, 238–247 (1991).